

Single-step Inkjet Printing PDMS Microlens Arrays for Tunable-Focus Artificial Compound Eyes

Shiyu Zhou, Hao Guo, Bo Qian, Lingying Li, Xuejun Shi

Shiyu Zhou

School of Nano Technology and Nano Bionics, University of Science and Technology of China, Suzhou 215123, China;

Hao Guo, Bo Qian, Lingying Li

Key Laboratory of Multifunctional Nanomaterials and Smart Systems, Suzhou Institute of Nano-Tech and Nano-Bionics, Chinese Academy of Sciences, Suzhou 215123, China;

Xuejun Shi

School of Physical Science and Technology, Soochow University, Suzhou 215006, China;

E-mail: bqian2010@sinano.ac.cn

Abstract

Flexible, tunable-focus artificial compound eyes (ACEs) have been extensively studied due to their large field of view (FOV), variable focal length, and large depth of field. The fabrication of flexible polydimethylsiloxane (PDMS) microlens arrays (MLAs) is a key issue for this system. Due to the difficulty of directly precision-machining PDMS, PDMS MLAs typically need molds, which involve complex, costly, and hard-to-control methods like laser fabrication and lithography. In this paper, a moldless, single-step inkjet printing method for PDMS MLAs is proposed. By optimizing the rheological

properties of the PDMS ink and adjusting printing waveforms, voltages, and frequencies, this study achieves, for the first time, large-scale inkjet printing fabrication of PDMS MLAs. The surface morphologies of the microlenses are uniformly consistent, resembling spherical caps. Subsequently, the optimized printed PDMS MLA film was bonded to a microfluidic chip to fabricate a hydraulically-driven, variable-focus ACE with the FOV tunable between 0 and 140° and the focal length tunable from 6mm to infinity. The ACE was demonstrated to image the objects at various distances by altering the volume of the injected liquid and possessing good optical imaging quality.

Key words: Polydimethylsiloxane (PDMS), Microlens Arrays, Inkjet Printing, Artificial Compound Eye, Variable-Focus imaging

1. Introduction

Eye morphology is fundamental to how animals see because it sets physical limitations on their capacity to form images ^[1]. Unlike the camera-type eyes humans possess, the natural compound eyes of arthropods consist of numerous closely packed and hemispherically distributed ommatidia, which individually direct light onto photoreceptors ^[2]. This eye morphology features small size, wide field-of-view (FOV), distortion-free imaging, and sensitive motion tracking ability, which inspires the innovation of imaging applications based on artificial compound eyes (ACEs), such as medical endoscopy, panoramic imaging, robot vision, and autonomous navigation ^[3].

However, most ACEs have fixed focal length and FOV, which limits the capability of distinguishing objects at different distances and the applications of variable-focus imaging. In order to overcome these limitations, tunable ACEs were further researched, which can achieve highly adaptive imaging performance by changing the geometric profile of lenses ^[4]. Among the different driving mechanisms for tunable ACEs, altering the pressure of the optical fluid encapsulated within the elastic film to modify the shape of the elastomer-fluid compound eye is a simple and flexible tuning strategy. In such a system, the key part is a flexible film with microlens arrays (MLAs) ^[5].

Polydimethylsiloxane (PDMS), as a low-cost and mechanically tunable transparent elastomer, is the most commonly used material for MLA films of tunable ACEs [6]. However, PDMS patterning usually needs molds, and the optical-grade surface quality requirement of the PDMS microlens further increases the difficulty of the fabrication processes, which leads most PDMS MLA films rely on complex microfabrication techniques. For example, the wet-etching-assisted femtosecond laser direct writing was used to fabricate Si or SiO₂ concave molds as the templates of soft lithography to prepare PDMS MLAs [7]. Xu et al. proposed another multi-step PDMS MLA fabrication method by preparing a micro-pillar array by photolithography, spin-coating UV resin onto the pillar array to generate concave molds [8], and finally replicating PDMS MLAs on these molds. Besides, thermal reflow, nano-sphere self-assembly, and ultraprecision machining processes are also used in the preparation of PDMS ACEs [9]. As mentioned above, most PDMS ACEs fabrication methods require the sophisticated preparation processes of mold and precise PDMS replication processes of micro-hemispherical shapes, which are complex, expensive, and time-consuming. Moreover, since these methods do not allow direct modification of the shape of the PDMS structure, it will greatly increase the fabrication cost of the molds with different lens geometries and packings.

Inkjet printing is a low-cost, non-contact, and digital technology that has been widely used in the preparation of optical devices, including microlens, waveguides, and integrated lasers [10]. Furthermore, drop-on-demand (DOD) inkjet printing allows precise control of ink deposition volume, enabling the creation of micro-spherical shapes with different curvatures by altering the number of drops per lens. However, directly inkjet printing PDMS MLAs still remain challenge due to the difficulty of the development of the PDMS ink formulation suitable for inkjet, and no related result has been reported until now. Some works reported inkjet printing UV-cured inks to prepare hemisphere arrays, which were used as the template to fabricate PDMS MLAs after two reverse molds [11]. Some studies have explored the fabrication of curved MLAs by printing UV microlenses on PDMS substrates [12]. However, the mismatch in refractive

indices between the two materials may adversely affect the optical performance, and the lower elasticity of UV-cured microlenses compared to PDMS can lead to damage during deformation. Such indirect processes are also very complex and time-consuming and waste the advantages of inkjet technology.

In this paper, we developed and optimized the rheological properties of the PDMS inks. After adjusting the printing waveforms, voltages, and frequencies, large-scale, single-step inkjet-printed PDMS MLAs were demonstrated for the first time. By controlling the number of droplets printed for each MLA, MLAs with various geometrical shapes and sizes were prepared. The fabricated PDMS MLAs film was bonded with a microfluidic chip to prepare a hydraulically-driven, variable-focus ACE. Compared with the conventional molding techniques, the single-step method in this paper greatly increases the convenience for the programming of the surface contours, size, and arrangement of the MLAs on the compound eyes. The ACE can be precisely adjusted by controlling the volume of liquid in the injected chamber, which allows the large-range dynamic adjustment of the FOV and imaging plane of the ACE within seconds.

2. Results and Discussion

The schematics of the ACE fabrication process are shown in Figure 1. Initially, the PDMS ink was printed as a 30×30 microlens square array on a PDMS film. Then, the printed array was heated in an oven to remove solvent and complete PDMS crosslinking. After repeatedly optimizing the ink rheological properties, the printing and thermal treatment processes according to the microstructure morphology and optical performance measurement results, the uniformly consistent PDMS MLAs film was obtained. Finally, the optimized printed PDMS MLAs film was bonded with a microfluidic chip to form a hydraulically-driven, variable-focus ACE by spreading and curing the mixture of PDMS precursor and cure agent on the structure interface. With precise pressure and flow control, the ACE's shape and focal length can be continuously modified.

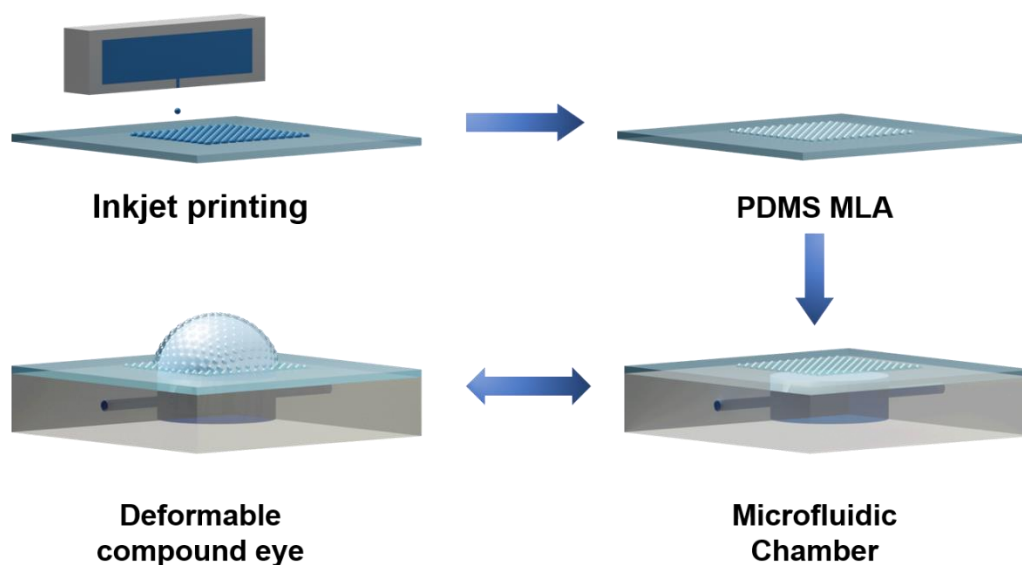


Figure 1. Schematics of the fabrication process of an ACE.

2.1. Inkjet Printing Fabrication of MLAs

The ink formulation is very important for inkjet printing processes, which directly influences the jetting stability, precision, and repeatability. The viscosity of the ink suitable for inkjet printing is usually in the range of 1-20 cP. However, due to the high viscosity, the mixture of PDMS precursor and curing agent cannot be directly used for inkjet printing. In this paper, we tried to add a low-viscosity solvent to the mixture of the PDMS precursor and curing agent to develop a PDMS ink suitable for inkjet printing.

Methylsiloxane is a kind of liquid organosilicon including hexamethyldisiloxane (MM), octamethyltrisiloxane (MDM), decamethyltetrasiloxane (MD₂M), dodecamethylpentasiloxane (MD₃M), and tetradecamethylhexasiloxane (MD₄M), which are usually used as excellent solvents or carriers for silicone oils or organosilicon materials ^[11b], and are promising to be the solvent for the PDMS ink. Following this idea, we performed the inkjet printing test with the PDMS inks diluted with the various linear methylsiloxanes, including MM, MDM, and MD₂M, respectively, and finally

found that only the ink diluted with MD₂M was jettable, which indicates that not only the low viscosity of the solvent but also the high boiling point of 194 °C at 760 mm Hg^[13] are very important for the inkjet inks.

To further optimize the MD₂M-based PDMS ink, inks with different PDMS concentrations were prepared, and their rheological properties were subsequently tested. Figure 2a shows the surface tension of the inks with different PDMS concentrations. It can be observed that with the PDMS concentration increasing, the surface tension fluctuates around 21 mN/m, indicating that the changes in the PDMS concentration have only a little bit of an impact on the ink's surface tension. Figure 2b shows the shear viscosity of the inks with different PDMS concentrations. At shear rates lower than 10 s⁻¹, the viscosity of each ink is slightly decreasing. At shear rates higher than 10 s⁻¹, the viscosities tend to be constant and increase from around 0.8 mPa·s to around 8.8 mPa·s, which indicates the Newtonian fluid property of the inks.

To determine which of the PDMS inks is suitable for inkjet printing, three dimensionless physical constants of the Reynolds (*Re*), Weber (*We*), and Ohnesorge (*Oh*) numbers were employed to characterize the inks^[14], with the definitions as shown in the following formulas respectively:

$$Re = \frac{v\rho a}{\eta} \quad (1)$$

$$We = \frac{v^2\rho a}{\gamma} \quad (2)$$

$$Oh = \frac{\sqrt{We}}{Re} = \frac{\eta}{(\gamma\rho a)^{\frac{1}{2}}} \quad (3)$$

Where, v (m s⁻¹) is the drop velocity, η (mPa s) is the viscosity, γ (mN m⁻¹) is the surface tension, ρ (g ml⁻³) is the density, and a (μm) is the nozzle diameter. *Re* represents the ratio between inertial and viscous forces in a moving fluid, while *We* depends on the ratio between inertia and surface tension. The *Oh*, defined as the ratio of *Re* to *We*,

encapsulates the interplay of viscous, inertial, and surface tension forces in a fluid. Typically, the Z number, which is the reciprocal of the Ohnesorge number ($Z = 1/Oh$), is employed to delineate the printable range of ink, which is $4 \leq Z \leq 14$ ^[14a]. Using the measured densities of the five PDMS inks, the Z numbers for the inks with the PDMS concentrations of 0, 5, 10, 15, 20 wt% are 24.66, 11.46, 4.77, 3.45, and 2.35, respectively (Table S1). It can be found that only the Z values of 5% and 10% PDMS inks fall within the printable range. Thus, we selected the 10 wt% PDMS ink to print the MLAs.

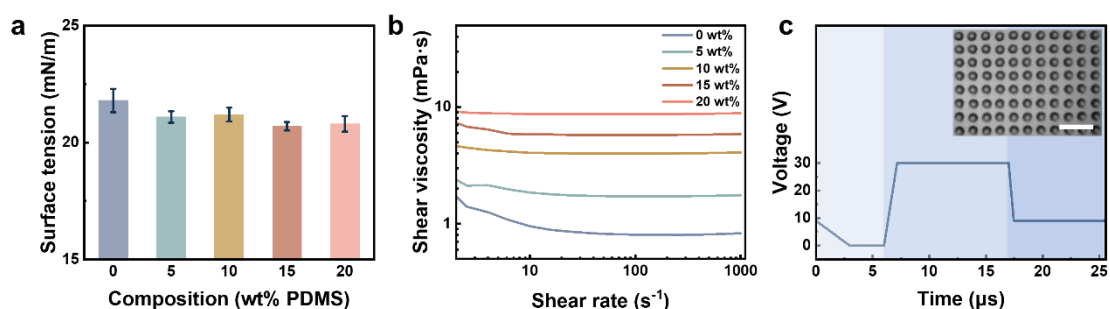


Figure 2. (a) Measured surface tensions of different inks. (b) Shear rate dependent viscosities of different ink compositions. (c) Waveform used for ink printing and the microscope image of an MLA arranged in a square layout. Scale bar: 500 μm .

Due to the low surface tension of the PDMS ink, Rayleigh instability occurs during inkjet printing, leading to an increase in satellite droplets and oscillations at the liquid surface of the nozzle, making it challenging to maintain a stable meniscus in a non-ejection state ^[15], which may result in low print quality as shown in Figure S4. To improve the print stability, the printing waveform was optimized as shown in Figure 2c. The waveform can be divided into three parts: (I) In the first part, the voltage drops from 9 to 0 volts when the time changes from 0 to 3 μs , and then the voltage maintains 0 volts from 3 to 6 μs . A lower positive voltage slope reduces fluid inertia forces, stabilizes the meniscus, and avoids possible air bubble introduction. (II) In the second part, the voltage increases from 0 to 30 V when the time changes from 6 to 7.15 μs (the voltage rising slope $\approx 26.09 \text{ V}/\mu\text{s}$), then stays at 30 V for 9.85 μs . The duration time of

the maximum voltage was designed to be about 3.5 times longer than that for the standard waveform in order to ensure the droplet is broken simply by the nozzle plate, which is important to reduce the possibility of satellite formation and retraction of air bubbles for low surface tension inks. (III) In the third part, voltage decreases from 30 to 9 volts when time changes from 17 to 17.45 μs and a 9 volt platform from 17.46 to 25.6 μs . The decreasing slope is 45.65 V/ μs , which is considering the faster retraction of the low surface tension ink detached from the droplet without a long stay outside the nozzle plate. Finally, based on this waveform (refer to the supporting information for a detailed description of the waveform), we can stably print large-area PDMS MLAs. The inset in Figure 2c presents the optical photograph of the as-printed MLAs on a PDMS substrate, showing uniform, smooth, and spherical cap appearances.

Subsequently, the printed samples were heated in an oven at 150 °C for 1 hour to remove the solvent and complete PDMS cross-linking. By controlling the number of printed droplets, MLAs with a series of sizes and spherical cap shapes were obtained. The diameters and heights of the microlenses were measured using a laser-scanning confocal microscope, as shown in Figure 3a. It can be observed that with the number of printed droplets increasing from 10 to 100, the height of the microlenses increases from 1.2 to 4.6 μm , and the diameter increases from 64.2 to 147.1 μm . Based on the spherical cap shapes of the microlenses, as determined by measurements, the focal length (f) and numerical aperture (NA) were calculated using the measured heights (h) and diameters (D) of these lenses. The focal length is the distance from the center of the lens to the focal point and can be expressed as ^[16]:

$$f = -\frac{4h^2 + D^2}{8h(n - 1)} \quad (4)$$

Where, n represents the refractive index of the material, which in this case is the refractive index of PDMS, i.e., $n = 1.43$ at 632.8 nm ^[17].

Numerical aperture describes the light-gathering ability (concentration capability) and spatial resolution of a lens. A larger NA implies greater light flux and higher resolution.

NA can be approximated as ^[16]:

$$NA \approx n \frac{D}{2f} \quad (5)$$

Where, n represents the refractive index of the medium between the lens and the observed object.

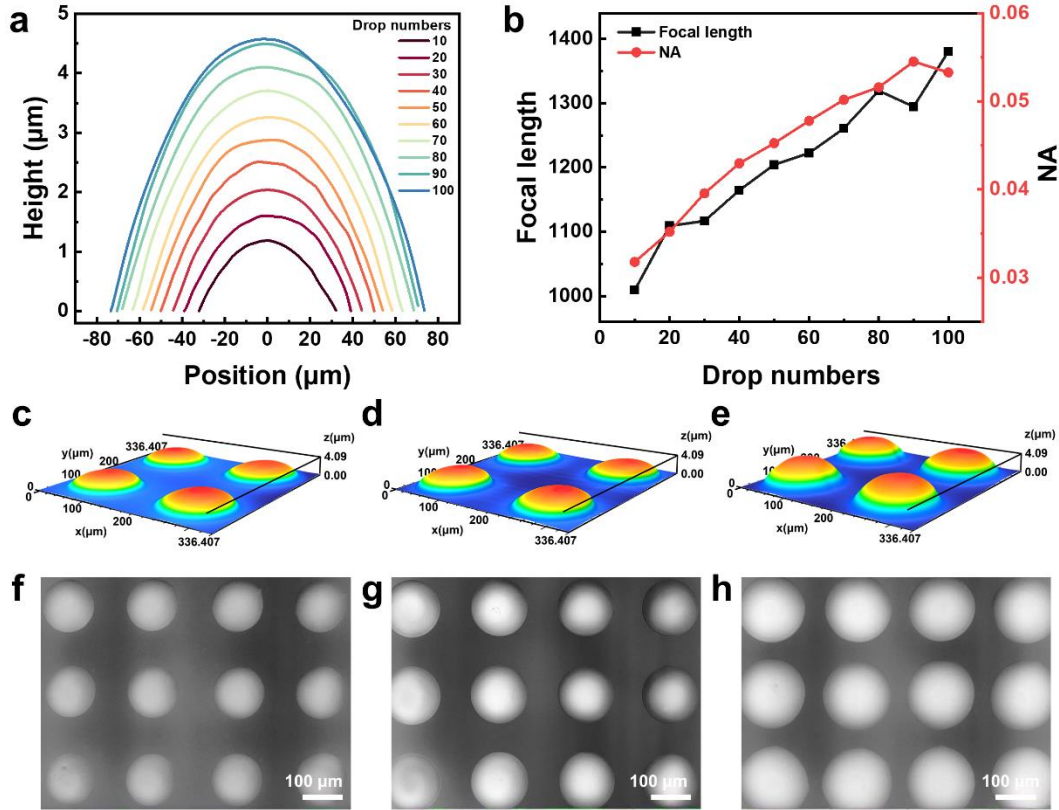


Figure 3. (a) Profiles of microlens for different drop numbers. (b) Focal length and numerical aperture for different drop numbers. (c-e) The 3D surface profile of the printed MLAs with drop numbers of (c) 60, (d) 80, (e) 100. (f-h) The microscope image of the printed MLAs with drop numbers of (f) 60, (g) 80, (h) 100. Scale bar: 100 μm .

Figure 3b shows the calculated focal lengths and NA of microlenses with varying droplet numbers. It can be observed that with the number of droplets increasing, the focal length gradually increases from 1009.4 μm to 1380.5 μm , and the NA increases from 0.03 to 0.05. This indicates that we can precisely adjust the focal length and NA of the microlens by simply controlling the number of printed droplets. The fluctuation

of the two curves is probably induced by the optical measurement error. Figure 3c-e presents the surface morphology of the PDMS MLAs with the printed droplet numbers of 60, 80, and 100, respectively, captured by the laser scanning confocal microscope. The smooth and consistent surface morphologies with different droplet numbers and different spherical cap shapes are further confirmed. Figure 3f-h shows the optical photographs corresponding to the samples in Figure 3c-e, respectively. It can be found that the degree of uniformity is slightly increased from Figure 3f to 3h, which indicates that more droplets will reduce the influence of the droplet jitter ^[18], and achieve higher structure uniformity.

2.2. Fabrication of ACEs

The MLAs film, featuring a 30×30 microlens array measuring 6×6 mm, was centrally bonded to the microfluidic chip to form an ACE. The dimension of the microfluidic chip is 20×20×5 mm³ (Figure S2). A 30 wt% calcium chloride (CaCl₂) aqueous solution was used as the filling optical liquid, with a refractive index of 1.43. Two soft pipes were connected to the in and out channels for the injection of the CaCl₂ aqueous solution. By controlling the flow of the injected optical liquid, the focal length of the ACE can be precisely adjusted.

Figures 4a and b show the optical and scanning electron microscope photographs of the MLA on the ACE, respectively. Note that each microlens was printed with 100 droplets, while the spacing between the microlens was designed at 200 μm. It can be observed that the microlenses are uniformly and orderly distributed on the top surface of the ACE in Figures 4b and c. The mean diameter of the microlenses was measured at about 150 μm. And the PDMS film was tightly bonded along the edge of the liquid reservoir. Note that 530 out of the total 900 microlenses above the liquid reservoir will contribute to the ACE imaging. Figure 4c shows the deformation process of the MLA PDMS film on the ACE. It can be observed that, due to the high elasticity of PDMS, the center film gradually bulges from a small curvature spherical cap to a large curvature hemisphere with the injection of more liquid. Note that the red dashed lines were drawn along the

upper profile of the ACE to facilitate the measurement of curvature radius (R), height (H), and bottom diameter (D). Figure 4e illustrates the injected liquid volume dependent focal length and FOV, which were calculated by the above mentioned formula 4 and the following formula 6 ^[19], respectively, according to the measured dimension values of the ACE in Figure 4d.

$$FOV = 2 \times \arcsin\left(\frac{2RH}{R^2} + H^2\right) \quad (6)$$

Theoretically, as the liquid volume increases, the focal length can be adjusted from infinity to 6 mm, while FOV expands from 0° to 180°.

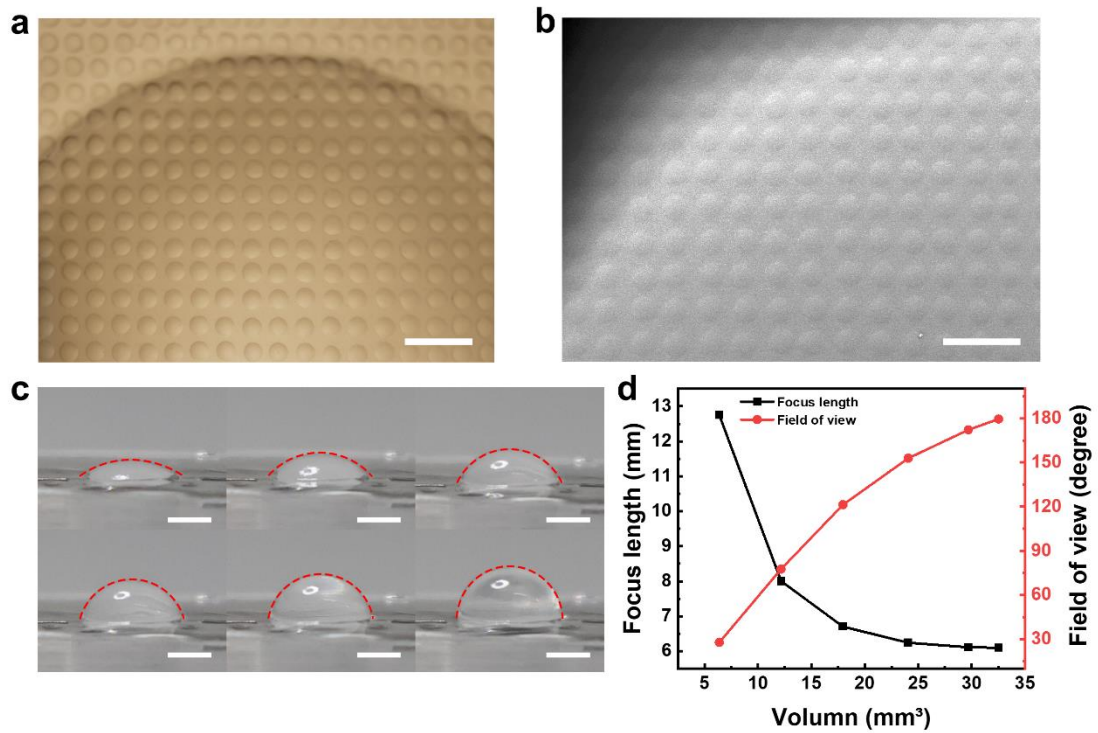


Figure 4. (a) The microscope image of the ACE. Scale bar: 500 μm. (b) The SEM image of the ACE. Scale bar: 500 μm. (c) The optical images of the ACE after injecting 6.38, 12.16, 17.96, 24.06, 29.68 and 32.52 mm³ CaCl₂ solution. Scale bar: 250 μm. (d) Liquid injection volume dependent focal length and FOV.

Figure 5a shows a schematic for the measurement of the FOV. The white light source was rotated around the ACE to adjust the incident angle, and the light received by the

ACE was captured by a charge-coupled device (CCD) camera. During this test, 32.52 mm³ of optical liquid was injected, resulting in a base diameter of 5 mm and a height of approximately 5 mm. As the incident angle increased from 0° to 70°, the amount of light collected by the ACE gradually decreased. When the incident angle exceeded 70°, the CCD camera captured no light, indicating that the maximum FOV of the ACE is 140°. Theoretically, the FOV of the ACE is calculated to be 180°. The discrepancy between the theoretical and measured values might be due to optical imperfections—the quality and uniformity of the optical liquid and the lens fabrication process can introduce imperfections that reduce the effective FOV—and scattering and absorption, where any scattering or absorption of light within the optical system can reduce the amount of light reaching the CCD camera at higher incident angles.

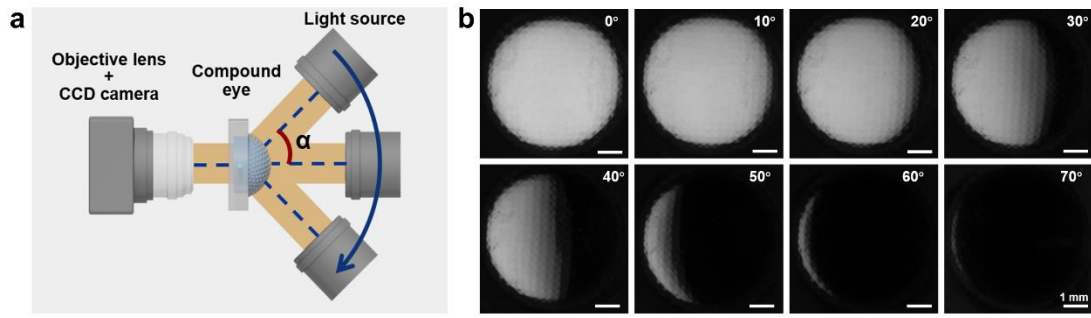


Figure 5. (a) Schematic illustration of the experimental setup for FOV characterization. (b) Images captured by the ACE at incident angles ranging from 0° to 70°. Scale bar: 1 mm.

2.3. Optical Characterization and Simulation of ACEs

The focusing effect characterization results are shown in Figures 6a-g, and the measurement setup is shown in Figure 6h. The measurement system used a 632.8 nm helium-neon (He–Ne) laser as the light source. An objective lens and a CCD camera were utilized to magnify and capture the images. The ACE was mounted on a sample stage, positioned between the light source and the objective lens, with its convex side oriented towards the camera. All the optical components were aligned along the same optical axis. In the absence of optical liquid within the ACE, the confocal image

obtained through the planar MLA is shown in Figure 6a. After injecting 6.65 mm^3 of optical liquid, the surface of ACE bulged into a spherical cap, each microlens of which can be regarded as an ommatidia on a compound eye, with the confocal image illustrated in Figure 6d. The intensity distribution of each focal point in Figures 6a and 6d was analyzed by MATLAB, as shown in Figures 6b, 6c, 6e, and 6f. Figures 6b and 6e illustrate the normalized light intensity distribution of the focal spots along the red dashed line in Figures 6a and 6d. Figures 6c and 6f display the 3D normalized light intensity distribution of all focal spots in Figures 6a and 6d, respectively. It can be observed that in the image captured by the planar MLA, the peak intensity heights of each focal point are similar, and they are evenly distributed in space. In the image captured by ACE, as the focal plane is a curved surface, the focal spots are concentrated in a circular region at the center, and the light intensity of the focal spots gradually diminishes from the center towards the periphery. Generally, the 3D peak intensity exhibits a centrally symmetric 3D Gaussian distribution.

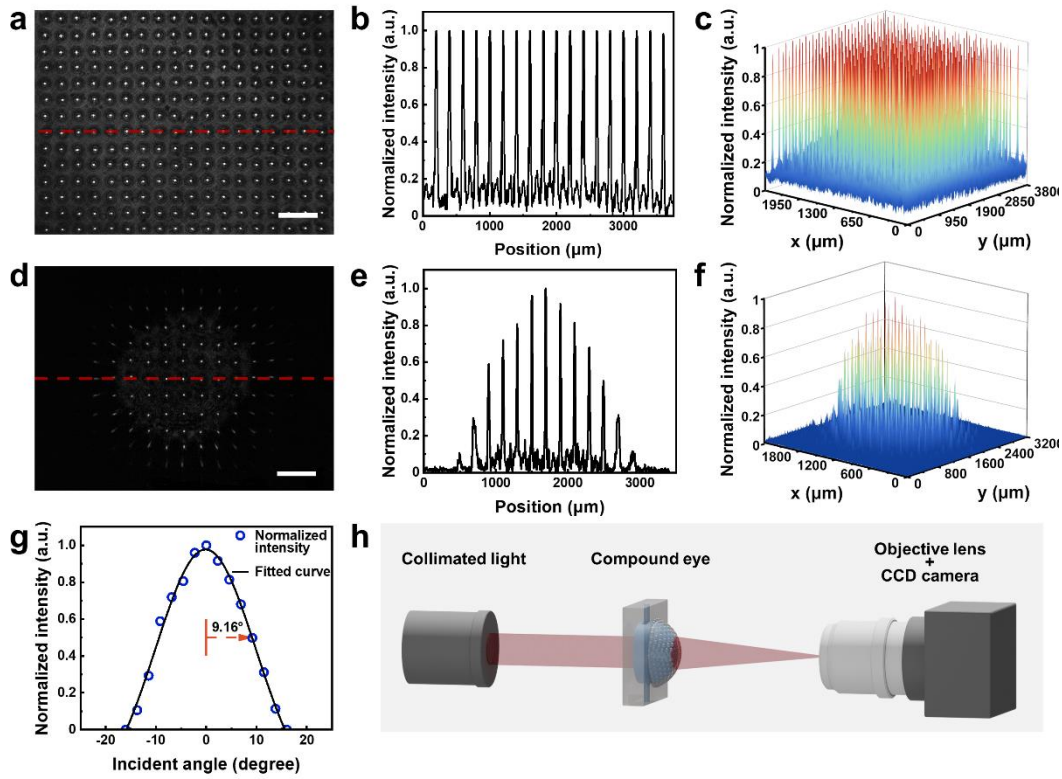


Figure 6. (a) Confocal image of the planar MLA. Scale bar: $500 \mu\text{m}$. (b) Normalized intensity distribution obtained along the red dotted line in (a). (c) 3D normalized

intensity distribution of all the focus spots in (a). (d) Confocal image of the ACE with 6.65 mm³ CaCl₂ solution injection. Scale bar: 500 μm. (e) Normalized intensity distribution obtained along the red dotted line in (d). (f) 3D normalized intensity distribution of all the focus spots in (d). (g) Angular sensitivity functions of the ACE. (h) Schematic illustration of the experimental setup for focusing effect.

Owing to the hemispherical arrangement of the ommatidia, the angle at which the incident laser couples into each ommatidium varies. The Angular Sensitivity Function (ASF) can be used to describe the sensitivity of ommatidia to light at different incident angles, serving as a crucial parameter for evaluating the visual perception capabilities of a compound eye in different directions^[20]. When injecting 6.65 mm³ of optical liquid, the ASF curves are plotted in Figure 6g based on the calculated incident light angles for each focal point in Figure 6e and their corresponding normalized light intensity values. The ASF curve follows a Gaussian distribution by theoretical fitting with the full width at half-maximum (FWHM) of 17.82°, which is defined as the acceptance angle of the ACE. The acceptance angle of a compound eye refers to the angular range for each ommatidium to receive incident light, associated with the arrangement of ommatidia, and it is a crucial geometric parameter for assessing the imaging capability of a compound eye. In addition to the acceptance angle, another important geometric parameter for evaluating imaging capability is the interommatidial angle. The interommatidial angle ($\Delta\phi$) is defined as the angle between the optical axes of adjacent ommatidia, influenced by the density of ommatidia in each region. The higher the density in the same area, the higher the visual acuity. Due to the isotropic deformation of the MLA film, the microlenses maintain a uniform distribution on the spherical surface after injecting optical liquid. The interommatidial angle can be calculated using the formula 7.

$$\Delta\phi = \frac{2d}{L} \arcsin \frac{L}{2R} \quad (7)$$

where d is the spacing between microlenses on the plane, L is the diameter of the

spherical cap, and R is the curvature radius of the ACE (Figure S5). Calculating with the parameters of the sample used in this study ($d = 0.2$ mm, $D = 5$ mm, and $R = 5$ mm), the value of $\Delta\varphi$ is determined to be 2.40° , which is quite smaller than the acceptance angle. Equation 7 indicates that the numerical value of $\Delta\varphi$ is inversely proportional to R with constant values for d and L . The calculated range of $\Delta\varphi$ for the sample used in this study spans from 1° to 7.2° , which is smaller than the acceptance angle (Figure S6). A smaller interommatidial angle can enhance visual resolution, but when the interommatidial angle is less than the acceptance angle, optical overlapping may occur between adjacent microlenses.

For better understanding the evolution of the light focusing process in the tunable ACE, we modeled and simulated the entire process using the COMSOL finite element analysis software, which involves the fluid-solid interaction and the ray tracing modules. To simplify the calculations, a two-dimensional model was used. Figure 7a shows the stress distribution of the ACE under a hydraulic pressure of 45 kPa. It can be observed that the film is spherical cap-shaped, which is consistent with the experiment. The stress of the upper spherical cap film is generally homogeneously distributed and about 50 kPa, which is close to the liquid pressure. This indicates the excellent elasticity of the PDMS film. Figure 7b displays the profile curves of the ACE's outer surface under different hydraulic pressures. It can be observed that as the pressure increases, the curvature radius of the ACE's surface decreases. Figure 7b also displays the profile of the microlenses on the top surface of the film under a hydraulic pressure of 6.4 kPa, which shows that the microlenses uniformly conform to the curvature of the ACE's outer surface. Based on the flat and curved film profiles, the incident light rays were traced, as shown in Figures 7c and 7d, respectively. In Figure 7c, through the flat MLAs film, the light rays are focused on a flat focal plane with a focal length of 14 mm. For the bulged MLA film in Figure 7d, the light rays are focused on a curved focal plane. This explains the focal light intensity Gaussian distribution observed in Figures 6d–f. Due to the mismatch between the curved focal plane of the bulging ACE and the flat focal plane of the CCD camera, if the center focal spots are in focus, the edge focal

spots will be out of focus, and vice versa. Note that the curvature radius of the focal plane in Figure 7d is significantly smaller than that of the bulging film. This is due to the incident angle-dependent refracting angle difference based on Snell law.

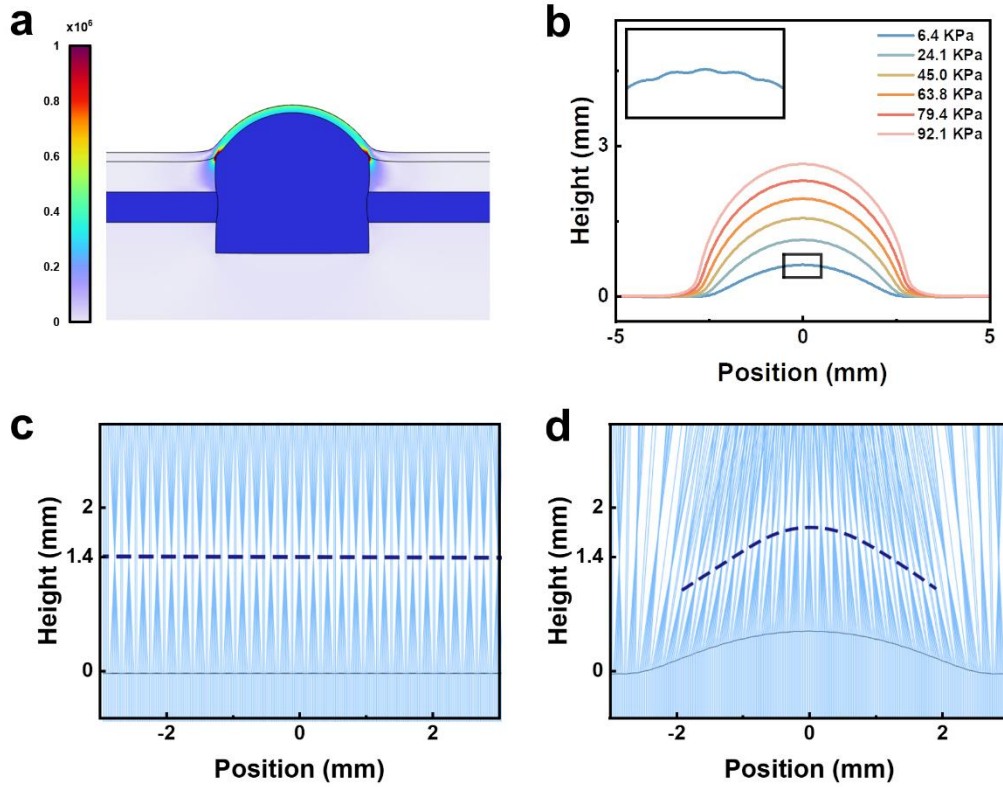


Figure 7. (a) Simulated stress distribution of the ACE. (b) The profile curves of the ACE's outer surface under different hydraulic pressures and the enlarged surface profile of the microlenses in the inset. (c) Ray tracing of flat MLA film. (d) Ray tracing of bulging MLA film. The dashed lines are the eye-guiding lines for the focal planes.

To investigate the imaging performance of the ACE, an optical imaging system was set up as shown in Figure 8a. A white-light-emitting diode (LED) served as the light source. An image mask featuring the letter 'F' was positioned between the light source and the ACE. The convex side of the ACE faced the camera. A CCD camera equipped with an objective lens was used to magnify and obtain the images. All components were aligned along the same optical axis. A volume of 6.19 mm^3 of CaCl_2 aqueous solution was injected into the ACE, with the volume being maintained throughout the measurement

process. Owing to the constant volume, the surface curvature and working distance of the ACE remained consistent. Due to the curved focal plane of the ACE, clear images could be captured at different positions on the curved surface by adjusting the distance between the ACE and the objective lens. Figure 8b presents a partial view of captured images, showing noticeable variations in the clarity of the letter "F" at different positions. Figures 8c-e present the images captured at the distances of 1.02, 0.90, and 0.77 mm between the ACE and the objective lens, respectively. The clarity of Figures 8c-e was quantified using MATLAB, with the results presented in Figures 8f-h. The clarity assessment of the "F" images captured by each ommatidium was conducted using the energy gradient function, followed by the normalization of the assessment results (refer to the supporting information for detailed calculation procedures). Each square in the figure represents the clarity analysis result of an individual "F" image, with brighter colors indicating higher clarity and darker colors indicating lower clarity. When the objective lens is positioned at a distance of 1.02 millimeters from ACE, the lens focuses on the top of the ACE sphere, resulting in the central region of the captured images being clearer than the periphery. As the distance between the objective lens and ACE decreases, the focus gradually moves towards the periphery, causing images with higher clarity to shift from the center to the edges. When the objective lens was positioned at a distance of 1.02 mm from the ACE, it focused on the top of the spherical cap, resulting in the central region of the captured images being clearer than the periphery. As the distance between the objective lens and ACE decreased, the focus gradually shifted towards the periphery, causing images with higher clarity to shift from the center to the edges.

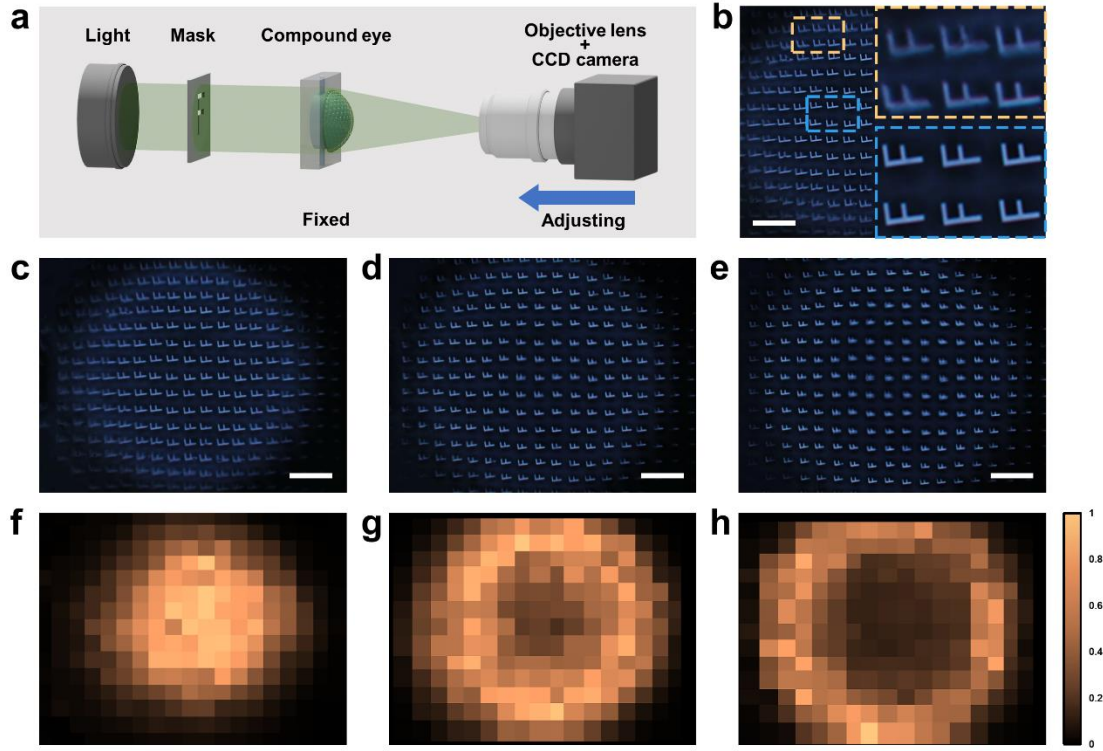


Figure 8. (a) Schematic illustration of the experimental setup for imaging performance. (b) Optical microscopic image of “F” with low and high clarity. Scale bar: 500 μm . (c-e) Optical microscopic images when the distances between the objective and the ACE are (c) 1.02 mm, (d) 0.90 mm, and (e) 0.77 mm. Scale bar: 500 μm . (f-h) The corresponding normalized definition image of (c-e). The color scale represents the clarity level of the “F” images. The image is clearest when the value is 1.

The test system for evaluating the tunable imaging capability of the ACE is depicted in Figure 9a. During this experiment, the positions of the objective lens and the ACE remained fixed, with adjustments made solely to the injected optical liquid volume. Figure 9b presents images captured by the planar MLA, showing the similarity in clarity for each “F” image captured by individual microlenses. Figures 9c-e display images obtained when the injected volumes are 4.81, 6.07, and 8.10 mm^3 , respectively, with the quantified clarity results depicted in Figures 9f-h. When the liquid volume in ACE amounted to 4.81 mm^3 , the curvature of the focal plane was relatively small, resulting in the region of clear imaging located at the center. As the liquid volume increased, the curvature of ACE gradually enlarged, causing the region of clear imaging to move from

the center towards the periphery, forming a circular area. Therefore, without changing the position of ACE, adjusting the injected volume of optical liquid allows for obtaining high-resolution images from different ommatidia.

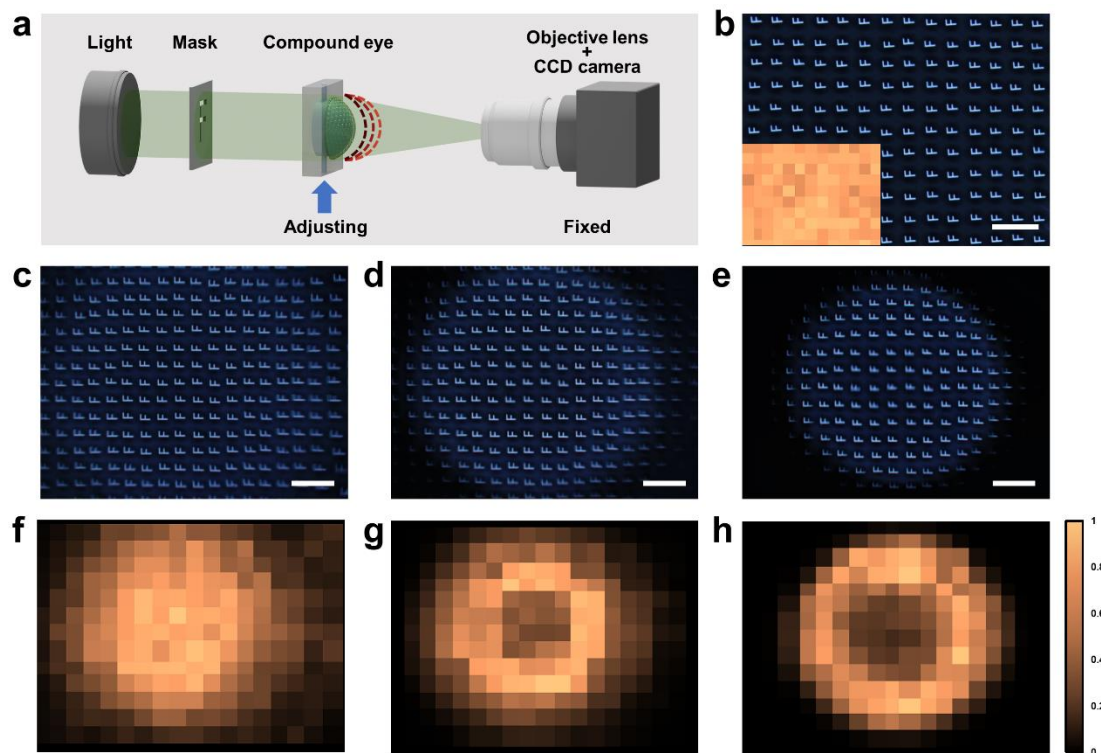


Figure 9. (a) Schematic illustration of the experimental setup for tunable imaging. (b) Optical microscopic image of the planar MLA and the corresponding normalized definition image. Scale bar: 500 μm . (c-e) Optical microscopic images of tunable ACE when the liquid volumes are (c) 4.81 mm^3 , (d) 6.07 mm^3 , (e) 8.10 mm^3 . Scale bar: 500 μm . (f-h) The corresponding normalized definition image of (c-e). The color scale represents the clarity level of the “F” images. The image is clearest when the value is 1.

3. Conclusions

In conclusion, this paper first proposes a single-step method for inkjet printing of PDMS MLAs based on the development of the PDMS ink and the driving waveform. This method significantly simplifies the manufacturing process of PDMS MLAs.

Compared to the traditional soft lithography method used for fabricating PDMS microlenses, this approach does not require additional molds or templates, allowing for simple and flexible customization and large-scale production. Secondly, the printed PDMS MLA is bonded with a microfluidic chip to fabricate a hydraulically-driven, variable-focus ACE. The FOV of the ACE can be adjusted between 0 and 180°, and the focal length can be adjusted within a range greater than 6mm. The proposed ACE, capable of imaging objects at various distances by altering the volume of injected liquid, possesses good optical imaging quality and can be applied in optical systems requiring a wide FOV and variable focus.

4. Experimental Section

Ink Preparation: The inks were designed with the PDMS precursor, curing agent (Sylgard 184, Dow Corning, USA), and decamethyltetrasiloxane (MD₂M) (Dowsil OS-30, Dow Corning, USA). The PDMS precursor and the curing agent were mixed with a weight ratio of 10:1. Then, the mixture was diluted in MD₂M with varying weight ratios (0%, 5%, 10%, 15%, and 20%). Note that for the convenience of description, the PDMS concentration in this paper means the concentration of the mixture of PDMS precursor and cure agent with a ratio of 10:1. After that, each solution was stirred for three minutes at 2000 rpm to achieve a homogeneous mixture.

MLA Fabrication Using Inkjet Printing: For the fabrication of the PDMS substrate, the PDMS precursor and curing agent were also mixed with a weight ratio of 10:1 and subsequently degassed in a vacuum desiccator for 30 minutes. The degassed PDMS mixture was then spin-coated on silicon wafers at 500 rpm for 20 seconds, resulting in a uniform thickness of approximately 200 μm. Subsequently, the PDMS substrate was cured in an oven at 100 °C for 30 minutes.

PDMS ink was printed using a SciZntics3 microelectronic printer (Shanghai Mifang Electronic Technology Co., Ltd.) equipped with a 10 pL printhead (FujiFilm Dimatix DMC-11610) and a nozzle diameter of 21 μm. During printing, the jetting frequency

was maintained at 500 Hz, and a customized jetting waveform was employed to ensure stable ink-jetting at this frequency. The number of ink drops for each microlens was adjusted by regulating the printing passes to control the geometric profile of the microlens on the PDMS substrate. Following that, the printed sample was placed in an oven at 150 °C for one hour to remove the solvent and complete PDMS cross-linking.

Compound Eye Fabrication: The ACE comprises a PDMS MLA film and a microfluidic chip. The microfluidic chip was prepared by PDMS casting with the PDMS precursor and cure agent weight ratio of 8:1. Note that increasing the cure agent content can enhance the elastic modulus of the PDMS polymer ^[21]. The casting mold was prepared by a polished glass substrate and a framework printed by a Fused Deposition Modeling (FDM) 3D printer. (Figure S1.) After the casting and solidification of PDMS in the mold, a PDMS microfluid chip (20 mm×20 mm×5mm) with a center circular liquid reservoir (5 mm in diameter, 3 mm in height) and two in and out fluid channels was formed. Subsequently, the PDMS MLA film was detached from the silicon wafer and bonded above the center reservoir of the microfluidic chip.

To match the refractive index of PDMS (1.43), a solution of deionized water (DI) and calcium chloride (CaCl₂) in a 7:3 mass ratio was injected into the channels of the microfluidic chip ^[22]. The transformation of the flexible MLA film from a planar to a hemispherical surface result in the formation of an ACE. Adjusting the volume of the injected liquid enables alteration of the focal length and FOV of the ACE.

Characterization: The viscosities of the inks were measured by a Kinexus Lab+ rheometer (NETZSCH Instruments, UK). The surface tensions of the inks were measured by a surface tensiometer (QBZY, Fangrui Instrument, China). The geometric dimensions and surface morphologies of both planar and curved states of the MLAs film were characterized by a VK-X250 laser scanning confocal microscope (Keyence, Japan) and a Quanta FEG 250 scanning electron microscope (FEI, USA). The optical micrographs characterizing the optical performance of the ACEs were obtained by a

BX51 optical microscope (Olympus, Japan). Digital images of the ACEs were captured by an EOS R50 compact mirrorless camera (Canon, Japan).

Supporting Information

Supporting Information is available from the Wiley Online Library or from the author.

Acknowledgements

The authors gratefully acknowledge financial support by R&D Plan for Key Areas of Guangdong Province (No. 2018B090905002), National Natural Science Foundation of China (No. 61575216), Key R&D programs in Jiangsu (No. BE2017082) and Suzhou Science and Technology Program (No. SYG201850).

Reference

- [1] P. A. T. Morris, *Zoological Journal of the Linnean Society* **2012**, 166, 912.
- [2] a) L. C. Kogos, Y. Li, J. Liu, Y. Li, L. Tian, R. Paiella, *Nature Communications* **2020**, 11, 1637; b) J. P. Currea, Y. Sondhi, A. Y. Kawahara, J. Theobald, *Communications Biology* **2023**, 6, 246; c) Z.-Y. Hu, Y.-L. Zhang, C. Pan, J.-Y. Dou, Z.-Z. Li, Z.-N. Tian, J.-W. Mao, Q.-D. Chen, H.-B. Sun, *Nature Communications* **2022**, 13, 5634; d) S. Sponberg, J. P. Dyhr, R. W. Hall, T. L. Daniel, *Science* **2015**, 348, 1245.
- [3] a) J. Li, S. Thiele, B. C. Quirk, R. W. Kirk, J. W. Verjans, E. Akers, C. A. Bursill, S. J. Nicholls, A. M. Herkommer, H. Giessen, R. A. McLaughlin, *Light: Science & Applications* **2020**, 9, 124; b) H. Jian, J. He, X. Jin, X. Chen, K. Wang, *Applied Optics* **2017**, 56, 1296; c) W.-B. Lee, H.-N. Lee, *Optics Communications* **2018**, 412, 178; d) C.-Y. Fan, C.-P. Lin, G.-D. J. Su, *Scientific Reports* **2020**, 10, 15677; e) G. C. H. E. de Croon, J. J. G. Dupeyroux, S. B. Fuller, J. A. R. Marshall, *Science Robotics* **2022**, 7, eabl6334.
- [4] a) A. Shahini, H. Jin, Z. Zhou, Y. Zhao, P.-Y. Chen, J. Hua, M. M.-C. Cheng, *Bioinspiration & Biomimetics* **2017**, 12, 046002; b) Z.-C. Ma, X.-Y. Hu, Y.-L. Zhang, X.-Q. Liu, Z.-S. Hou, L.-G. Niu, L. Zhu, B. Han, Q.-D. Chen, H.-B. Sun, *Advanced Functional Materials* **2019**, 29, 1903340; c) C. Liu, Y. Zheng, R.-Y. Yuan, Z. Jiang, J.-B. Xu, Y.-R. Zhao, X. Wang, X.-W. Li, Y. Xing, Q.-H. Wang, *Laser & Photonics Reviews* **2023**, 17, 2300274.
- [5] Y. Cheng, J. Cao, Y. Zhang, Q. Hao, *Bioinspiration & Biomimetics* **2019**, 14, 031002.
- [6] a) F. Liu, X. Diao, L. Li, Y. Hao, Z. Jiao, *Micromachines* **2018**, 9, 238; b) Y. Wang, C. Shi, C. Liu, X. Yu, H. Xu, T. Wang, Y. Qiao, W. Yu, *Journal of Micromechanics and Microengineering* **2019**, 29, 055008; c) K. Wei, H. Zeng, Y. Zhao, *Lab on a Chip* **2014**, 14, 3594.
- [7] a) J.-J. Cao, Z.-S. Hou, Z.-N. Tian, J.-G. Hua, Y.-L. Zhang, Q.-D. Chen, *ACS Applied Materials & Interfaces* **2020**, 12, 10107; b) H. Bian, Y. Wei, Q. Yang, F. Chen, F. Zhang, G. Du, J. Yong, X. Hou,

- Applied Physics Letters* **2016**, 109, 221109.
- [8] Q. Xu, B. Dai, Z. Jiao, R. Hong, Z. Yang, D. Zhang, S. Zhuang, *Optics Express* **2018**, 26, 33356.
 - [9] a) L. Li, A. Y. Yi, *Appl. Opt.* **2012**, 51, 1843; b) D. Shin, T. Huang, D. Neibloom, M. A. Bevan, J. Frechette, *ACS Applied Materials & Interfaces* **2019**, 11, 34478; c) J. Luo, Y. Guo, X. Wang, F. Fan, *Journal of Micromechanics and Microengineering* **2017**, 27, 045011.
 - [10] R. Magazine, B. van Bochove, S. Borandeh, J. Seppälä, *Additive Manufacturing* **2022**, 50, 102534.
 - [11] a) Z. Xiaoyang, C. Hejuan, Z. Li, W. Hongcheng, Z. Weiyi, *Optical Engineering* **2014**, 53, 117109; b) J. Li, W. J. Wang, X. S. Mei, D. X. Hou, A. F. Pan, B. Liu, J. L. Cui, *ACS Applied Materials & Interfaces* **2020**, 12, 8870.
 - [12] P. Zhou, H. Yu, Y. Zhong, W. Zou, Z. Wang, L. Liu, *Nano-Micro Letters* **2020**, 12, 166.
 - [13] G. Di Marcobertardino, C. M. Invernizzi, P. Iora, L. Arosio, M. Canavese, A. Lunghi, A. Mazzei, *Energies* **2022**, 15, 3498.
 - [14] a) D. Jang, D. Kim, J. Moon, *Langmuir* **2009**, 25, 2629; b) B. Derby, *Annual Review of Materials Research* **2010**, 40, 395.
 - [15] E. Antonopoulou, O. G. Harlen, M. Rump, T. Segers, M. A. Walkley, *Physics of Fluids* **2021**, 33, 072112.
 - [16] Q. Yang, M. Li, H. Bian, J. Yong, F. Zhang, X. Hou, F. Chen, *Advanced Materials Technologies* **2021**, 6, 2100091.
 - [17] F. Schneider, J. Draheim, R. Kamberger, U. Wallrabe, *Sensors and Actuators A: Physical* **2009**, 151, 95.
 - [18] W. Wang, X. Zhu, L. Li, B. Qian, Y. Xie, *Journal of Physics D: Applied Physics* **2019**, 52, 315302.
 - [19] D. Wu, J.-N. Wang, L.-G. Niu, X. L. Zhang, S. Z. Wu, Q.-D. Chen, L. P. Lee, H. B. Sun, *Advanced Optical Materials* **2014**, 2, 751.
 - [20] a) C. Tan, X. Cai, Z. Luo, Z. Li, C. Xiu, Z. Chen, L. Bian, *Insects* **2023**, 14, 370; b) T. J. Wardill, S. T. Fabian, A. C. Pettigrew, D. G. Stavenga, K. Nordström, P. T. Gonzalez-Bellido, *Current Biology* **2017**, 27, 854.
 - [21] T. K. Kim, J. K. Kim, O. C. Jeong, *Microelectronic Engineering* **2011**, 88, 1982.
 - [22] C.-Y. Tan, Y.-X. Huang, *Journal of Chemical & Engineering Data* **2015**, 60, 2827.